nature physics

Article

https://doi.org/10.1038/s41567-026-03175-w

Kelvin wave propagation along vortex cores

Received: 2 June 2025

Accepted: 8 January 2026

Jason Barckicke[1,2], Eric Falcon[1] ✉ & Christophe Gissinger[2,3] ✉

Kelvin waves are the most fundamental excitations that propagate along vortex lines, and they play a central role in the redistribution of energy and the stability of rotating flows. They are believed to underpin key processes in both classical and quantum turbulence, from the decay of vortex tangles in superfluid helium to dissipation mechanisms in atmospheric vortices. Despite their importance, quantitative observations of Kelvin wave dynamics that resolve their dispersion relation remain a challenging problem. Here we experimentally characterize the propagation of Kelvin waves along a stable, controlled and macroscopic vortex core and access their dispersion relation. Our spatiotemporal measurements, spanning nearly two decades in scale, reveal both helical bending modes and double-helix waves, which validates theoretical predictions for turbulent rotating flows. We also observe the statistics of temporal fluctuations of Kelvin waves and show how their dynamics are shaped by local vortex properties, such as vertical flow and excitation location. Our results provide quantitative insight into the mechanisms driving energy cascades in Kelvin wave turbulence, thus offering a classical analogue to quantum systems in which direct measurements remain inaccessible. Beyond this fundamental relevance, they also shed light on the dynamics of large-scale vortices, from intermittent tornado behaviour to the stability of aircraft wake vortices.

Vorticity is fundamental in fluid dynamics, as it governs flows across diverse natural and engineered systems. From quantum turbulence to atmospheric cyclones and oceanic eddies, much of the observed complexity stems from vorticity dynamics. In classical and quantum turbulence, vorticity is concentrated along thin vortex lines. Kelvin waves are elementary excitations of a vortex line and are typically defined around ideal or smoothly varying vortices. They appear as velocity perturbations propagating along its core[1]. As such, they play a central role in energy redistribution, vortex stability and turbulent cascades[2].

Kelvin waves were first described in classical hydrodynamics. Modelling turbulent flows as vortex filaments interacting via Kelvin waves provides crucial understanding of their dynamics[3,4]. These waves affect vortex stability: wake vortices from aircraft wings, for example, can persist over long distances and pose hazards to trailing aircraft[5]. As they propagate, they influence vortex stability and breakdown, which impacts aviation safety[6]. Similarly, in atmospheric phenomena, Kelvin waves contribute to tornado propagation and intensification[7,8], thus mediating their natural variability[9] (the 'skipping effect').

Kelvin waves play a unique role in quantum fluids, such as superfluid helium and Bose–Einstein condensates, due to the quantized vorticity[10,11]. When these systems are rotated, a lattice of vortices forms aligned along the rotation axis, with circulation quantized by the Onsager–Feynman quantum[12,13] and core sizes theoretically ranging from angstroms in superfluid ^{4}He to micrometres in Bose–Einstein condensates[14]. Without molecular dissipation, quantum vortices reconnect, form tangles and trigger Kelvin weak-wave turbulence[15,16], which carries energy from the intervortex spacing down to the core scale[17–22]. Dissipation then occurs at smaller scales through quantum mechanisms like phonon emission.

However, substantial experimental challenges remain in both classical and quantum settings. Using advanced submicrometre particle visualization in superfluid ^{4}He, Kelvin waves on quantized vortices were directly observed only in 2013 (ref. 23). Yet, such experiments

---

[1]Université Paris Cité, CNRS, MSC, UMR 7057, Paris, France. [2]Laboratoire de Physique de l'Ecole Normale Supérieure, ENS, Université PSL, CNRS, Paris, France. [3]Institut Universitaire de France, Paris, France. ✉e-mail: eric.falcon@u-paris.fr; christophe.gissinger@phys.ens.fr

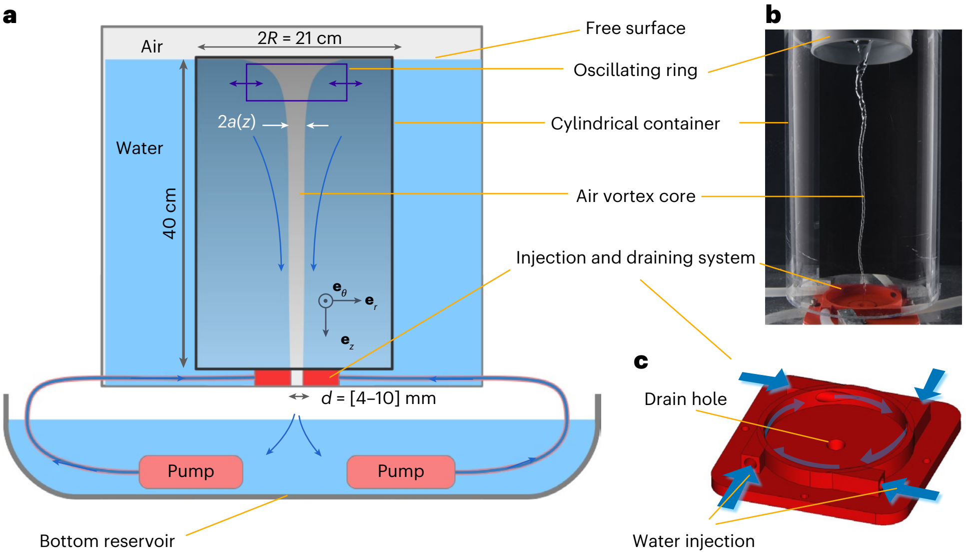

Fig. 1 | Experimental set-up for creating a stationary vortex. a, Experimental set-up. Here $\mathbf{e}_r$, $\mathbf{e}_\theta$ and $\mathbf{e}_z$ are the unit vectors of a cylindrical coordinate system. The figure shows a (r,z) cross-section, with $\mathbf{e}_\theta$ pointing out of the plane. **b**, Snapshot of a conical air column vortex with propagating helical Kelvin waves. **c**, The 3D-printed injection and draining system generates a circular flow at the bottom of the cylindrical container.

remain rare due to the nanoscale dimensions of vortex cores and difficulties in reliably exciting Kelvin waves under controlled conditions[24]. In classical fluids, their visualization is also challenging due to the thin, transient and intermittent nature of the waves. Despite impressive high-speed visualizations of straight and knotted vortex lines[25–27], the experimental validation of theoretical predictions has been limited, which limits our ability to gain a further understanding of Kelvin wave dynamics.

A key question remains: how can we experimentally characterize the Kelvin wave dispersion relation? Lord Kelvin first described these waves theoretically in 1880 (ref. 1), but later work revealed complex modes depending on the vortex structure[28]. Recent theoretical advances have accounted for intricate geometries and viscous effects[29,30], but the lack of experimental validation[24] leaves uncertainties on which modes contribute to energy cascades. Our measurements deliver experimental characterization of the Kelvin wave dispersion relation at high resolution, enabling a direct and quantitative connection between theoretical models and observed dynamics. We uncover a rich spectrum of Kelvin waves, including helical bending and double-helix flattening modes, in line with theoretical predictions[1,28]. The statistics of their temporal fluctuations offer insight into tornado dynamics. Finally, we highlight the influence of the helicity of the flow and the source location of perturbations, factors that are critical to vortex stability and energy dynamics in classical and quantum fluids.

Generating an air–water vortex line

Since Feynman's 1955 seminal work[11], modelling superfluid vortices is known to require a finite-sized core with confined vorticity. Two classic representations are the hollow-core (empty-core) and Rankine (core in solid-body rotation) models (Supplementary Information). These models consist of an irrotational flow with finite circulation, which is crucial for sustaining Kelvin waves, around a finite-sized core, hence reproducing vortex topology. A well-known relevant laboratory analogue is the bathtub vortex, in which swirling water drains through a hole at the bottom of a rotating tank to form a rapidly rotating vortex around an air core. This set-up is used to explore rotating flows in classical[31,32] and quantum[33] fluids, although it does not focus on Kelvin waves. Both models also capture key features of tornado dynamics.

Building on these models, we developed an experimental set-up to generate a stable, controlled, macroscopic (~0.4 m) vortex specifically designed to investigate Kelvin waves. As shown in Fig. 1, the set-up consists of a 21-cm-diameter, 45-cm-tall cylindrical tank in which a stationary vortex forms. The fluid undergoes angular rotation $\Omega(r)$, r being the radial coordinate. Unlike previous rotating-tank experiments, we create the vortex by injecting water via two pumps feeding four inlets placed symmetrically around a bottom drain hole (Fig. 1c). The vortex circulation Γ is controlled via the pump flow rate and drain size (diameter d, typically a few millimetres). A vibrating annulus shakes the vortex horizontally at the top. The air–water interface is imaged by an optical camera normal to the vortex axis, yielding precise measurements of the vortex-core radius $a(z,t)=[r(z,t,\theta=0)+r(z,t,\theta=\pi)]/2$ and horizontal displacement $\eta(z,t)=[r(z,t,\theta=0)-r(z,t,\theta=\pi)]/2$ (Methods). These profiles are Fourier-analysed to extract the Kelvin wave dispersion relation. The azimuthal and vertical fluid velocity profiles, $v_\theta(r)$ and v_z, are measured via particle image velocimetry (PIV) and particle-tracking velocimetry, respectively (Methods). Under suitable parameter settings, this set-up serves as an excellent laboratory model for studying vortex-line waves, as it closely reproduces the idealized conditions assumed in theoretical studies.

The flow from the four bottom injectors is confined within an external cylinder, which yields a very thin, tall and steady vortex (Fig. 1b and Supplementary Video 1). Owing to the pressure field within the fluid, which combines hydrostatic, dynamic pressure due to rotation and localized suction near the drain, the air-core radius $a(z)$ slowly increases with altitude, from ~1 mm near the drain to ~2 mm halfway up the tank. It then widens markedly just below the flat free surface. In comparison, the vortex height is typically 40 cm, two orders of magnitude larger than $a(z)$. The vortex profile is controlled by the pump flow U and the hole diameter d; increasing either deepens and widens the vortex (Fig. 2a,b). For wide enough holes, $v_\theta(r)$ decreases as $1/r$, as in a Rankine vortex (Fig. 2c). This model assumes ideal irrotational flow outside the core, that is, constant circulation $\Gamma\equiv 2\pi r v_\theta(r)$, as is roughly observed experimentally far enough from the core (Fig. 2d). Typical values are $\Gamma\approx 10^{-2}\,\mathrm{m^2\,s^{-1}}$. a_0 is approximately a few millimetres, giving a typical angular rotation of the water–air interface $\Omega_0\equiv\Omega(a_0)=\Gamma/(2\pi a_0^2)\approx 10^3\,\mathrm{s^{-1}}$. The non-dimensional wave parameters are $\omega/\Omega_0\in[0,0.4]$ and $|k|a_0\in[0,10]$. ω is the angular frequency of the wave perturbations and k their axial wavenumber. The vortex-core radius averaged in the vertical camera field $a_0\equiv\langle a\rangle_z$. Note that as Γ and v_z also depend on z, we use their average values in

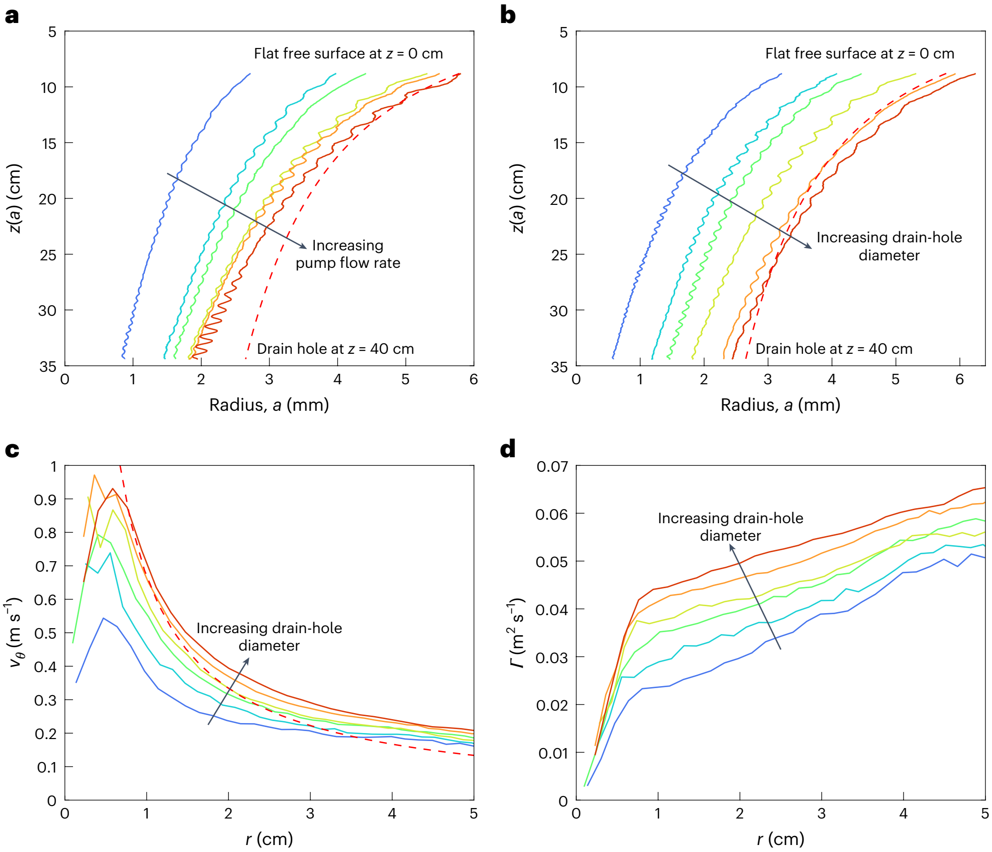

Fig. 2 | Time-averaged vortex profile and fluid velocity profile. **a**, Vortex profile $z(a)$ as a function of its radius a (from contour detection) for different pump flow rates $U \in [8, 13]$ V and fixed $d = 7$ mm. **b**, Vortex profile for different drain-hole diameters $d \in [4, 9]$ mm and fixed $U = 11$ V. Oscillations correspond to Kelvin waves. Red dashed lines correspond to the hollow-core Rankine vortex profile $z(a) = \Gamma^2/(8\pi^2 g a^2)$ with $g = 9.81$ m^2 s^{-1} and $\Gamma = 0.042$ m^2 s^{-1}. **c**,**d**, Fluid velocity profiles (from PIV measurements). Azimuthal velocity profile $v_\theta(r)$ (**c**) and circulation $\Gamma(r) = 2\pi r v_\theta(r)$ (**d**) within the liquid, for different $U = 11$ V and $d \in [4, 9]$ mm and at a depth $z = 25$ cm. The red dashed line corresponds to the Rankine vortex model: $v_\theta(r \geq a_0) = \Gamma/(2\pi r)$ with $\Gamma = 0.042$ m^2 s^{-1}. For **a** and **b**, the measurement uncertainty is negligible. For **c** and **d**, the measurement uncertainty is of the order of the fluctuation in r.

the theoretical calculations, given that they vary less than $a(z)$. Typically, the vertical velocity is $v_z \approx 0.5$ m s^{-1}.

Dispersion relation for Kelvin waves

In cylindrical coordinates (r, θ, z), linear theory predicts that a vortex aligned along the z axis can sustain Kelvin waves, with core-radius perturbation $r_c \equiv a_0 + \varepsilon \cos(kz + m\theta + \omega t)$, where $\varepsilon \ll a_0$ is the perturbation amplitude. Here $\omega = 2\pi f$ is the angular frequency, k the axial wavenumber and m the azimuthal wavenumber. Among these, bending waves ($m = 1$) feature a helical core displacement (Extended Data Fig. 1) with constant radius and spanning many length scales[28]. Such bending waves play a large role in energy transfer across scales in both classical and quantum fluids[34]. To observe them, we force the vortex via horizontal oscillations of the top annulus over a frequency sweep $f = 1$–6 Hz. This generates downward-propagating complex wavy structures, including helical bending waves (Fig. 3a and Supplementary Video 1).

Using spatiotemporal imaging, we tracked the vortex-core displacement $\eta(z, t)$ from the left-hand and right-hand sides of the core, both yielding consistent spectra. The experimental spatiotemporal spectrum in Fig. 3b quantitatively characterizes the Kelvin wave dispersion relation. One distinct branch spans nearly two decades in frequency and wavenumber, corresponding to waves clearly visible in Fig. 3a and propagating downward ($k > 0$). As this branch does not appear in the radius spectrum (see below), it corresponds to $m = 1$ waves. Using two orthogonal cameras, we evidenced that this $m = 1$ mode involves only counterrotating waves, as theory predicts[28].

In the long-wavelength limit ($ka_0 \ll 1$), the observed dispersion relation follows Kelvin's classical prediction with $m = 1$ for a hollow vortex[1]:

$$\omega(k) = -\frac{\Gamma}{4\pi} k^2 \left[\log\left(\frac{2}{ka_0}\right) - \gamma\right], \tag{1}$$

with $\Gamma = 2\pi a_0^2 \Omega_0$ the circulation and $\gamma \approx 0.577$ Euler's constant. $\omega < 0$ is consistent with counterrotating waves. For quantum fluids, Γ would correspond to the quantum of circulation $\kappa = h/M$, where h is the Planck constant and M is the mass of the particle[34]. This classical expression (red line in Fig. 3b) fits the data for $ka_0 \ll 1$ as expected, with parameters a_0 and Γ consistent with experimental values. However, at higher k, it fails because it neglects the vertical velocity v_z (even without the assumption $ka_0 \ll 1$)[34].

As no hollow-core model accounts for vertical flow, we adopt the (solid-body core) Rankine model with uniform vertical velocity v_z (refs. 1,28), taken positive for a downward flow. We assume an inviscid, incompressible flow with solid-body rotation and a uniform downward velocity v_z in the core ($r < a_0$) and irrotational flow outside. Adding infinitesimal velocity (and pressure) perturbations $u_i(r)\,\mathrm{e}^{\mathrm{i}(kz + m\theta + \omega t)}$ to the Euler equations and considering the continuity of velocity and pressure at the perturbed surface r_c leads to the dispersion relation defined by the classical transcendental equation[1,28]:

$$\frac{(\omega + m\Omega_0)^2}{4\Omega_0^2 - \tilde{\omega}^2}\left[\frac{\beta a_0 J'_{|m|}[\beta a_0]}{J_{|m|}[\beta a_0]} + \frac{2\Omega_0 m}{\tilde{\omega}}\right] = -a_0|k|\frac{K'_{|m|}[|k|a_0]}{K_{|m|}[|k|a_0]}, \tag{2}$$

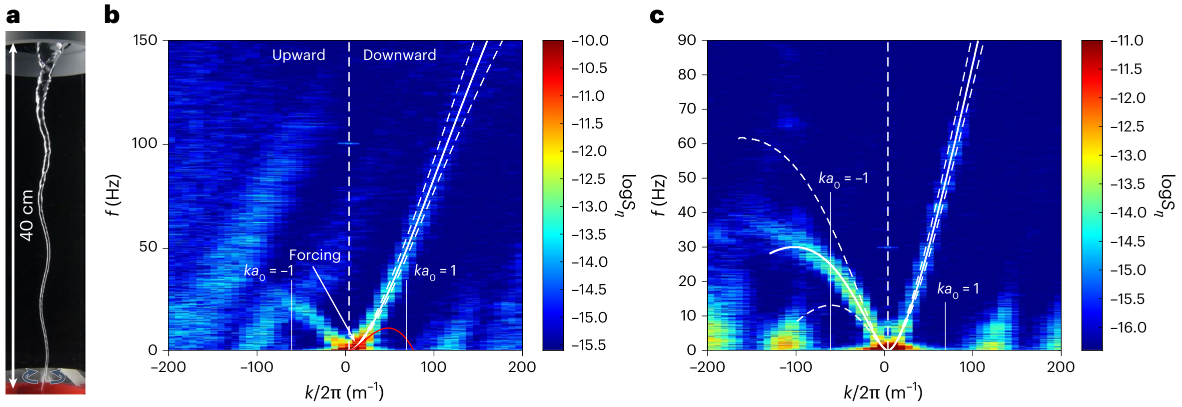

Fig. 3 | Helical bending mode (m = 1) of Kelvin vortex waves. a, Snapshot of counterrotating bending waves deforming the vortex axis. A sweep-sine forcing (1–6 Hz) located on the top generates downward ($k > 0$) Kelvin waves. The pump flow rate $U = 11$ V, and drain-hole diameter $d = 5$ mm. **b**, Corresponding spatiotemporal power spectrum of the vortex position S_η. The solid white line corresponds to the theoretical dispersion relation of $m = 1$ Kelvin waves of equation (2) with parameters $a_0 = 1.9$ mm, $\Gamma = 0.022$ m^2 s^{-1} and $v_z = 0.57$ m s^{-1}, consistent with experimentally measured values. The red line corresponds to the long-wavelength limit (equation (1)). **c**, Spatiotemporal power spectrum of the vortex position with the same parameters but with no external forcing. Upward (upstream) Kelvin waves ($k < 0$) are clearly observed and described well by equation (2) with the same experimental parameters (solid white line). Note that the branch of downward bending waves shown in **b** is still visible here (solid white line). To account for variations of the radius a with depth z, the white dashed lines in **b** and **c** correspond to equation (2) computed with $a_0 = \min[a(z)]$ (right) and $a_0 = \max[a(z)]$ (left).

where $\tilde{\omega} = \omega + m\Omega_0 + kv_z$ and $\beta = k\sqrt{4\Omega_0^2/\tilde{\omega}^2 - 1}$. J_m is the Bessel function of the first kind of order m, and K_m the modified Bessel function of the second kind. This equation involves the parameters $a_0 \equiv \langle a(z)\rangle$, Ω_0 and v_z, which can be directly obtained from experimental measurements for each run (Extended Data Figs. 2–4). This prediction (white line in Fig. 3b) fits our data very well using $a_0 = 1.9$ mm, $\Gamma = 0.022$ m^2 s^{-1} and $v_z = 0.57$ m s^{-1}, values consistent with measurements from contour detection, PIV and particle tracking, respectively (Methods).

Despite the axial variation of the vortex-core radius $a(z)$, the observed dispersion relation remains well described by the uniform-core model of equation (2), consistent with a local approximation valid in slowly varying media (Methods). Moreover, the white dashed lines in Fig. 3b,c correspond to the theoretical dispersion relation computed using the extremal values of $a(z)$ at the top and bottom of the measurement domain and keeping all other parameters constant. Equation (2) admits infinitely many solutions due to the behaviour of the Bessel functions. The $m = 1$ solution involving $\omega(k) \to 0$ as $k \to 0$ is especially robust, independent of core details and common to all vortex models, and it plays a key role in both classical and quantum fluids. It also falls within our accessible frequency range. This bending mode dominates the energy spectrum, particularly at low k, underscoring its role in turbulent cascades. Other weaker spectral features in Fig. 3b are reminiscent of modes $m \geq 2$ (discussed below).

Under specific conditions, a distinct dispersion branch emerges for $k < 0$ (Fig. 3c), which is dominant when the drain hole is small ($d \leq 6.5$ mm) and no external forcing is applied. Like their downward counterparts, these upward-propagating bending waves are helical disturbances, visible in position spectra but not in core-radius spectra, and are captured well by equation (2) for $m = 1$ and $k < 0$ (solid white line). Downward-propagating waves remain visible, albeit weaker without forcing, and follow the same dispersion relation of equation (2) (solid white line in Fig. 3c), with the same fitting parameters. The bending-wave dispersion branch differs for upstream and downstream waves because the vertical flow breaks the symmetry, as exemplified by the nearly vanishing group velocity of upstream waves at $|k|a_0 \approx 1$.

Notably, our set-up also reveals a second wave mode that does not displace the vortex axis and is, thus, distinct from $m = 1$ bending waves. As seen in Fig. 4a and Supplementary Video 2, double-helix ($m = 2$) structures propagate both up and down with wavelengths $\lambda \lesssim 1$ cm. These disturbances, called fluted or flattening waves[29,30], are $m = 2$ modes of Kelvin waves and involve core-radius variations without vortex-axis displacement, which explains their less intense observation in position spectra (Fig. 3).

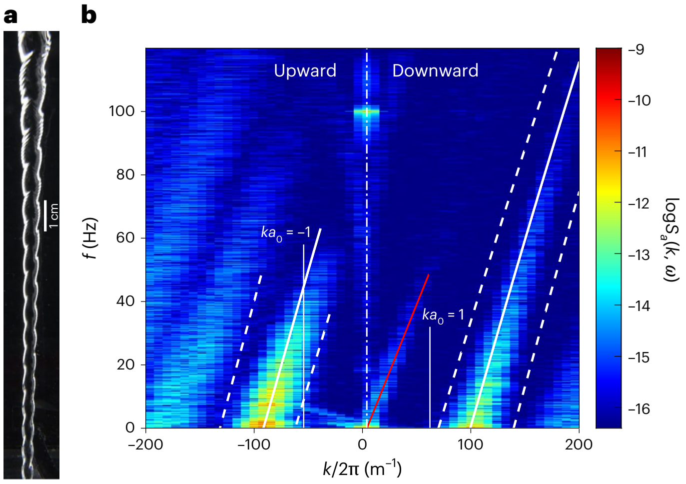

Fig. 4 | Double-helix flattening mode (m = 2) of Kelvin waves. a, Close-up view of $m = 2$ perturbations, also called a fluted Kelvin wave, which elliptically flattens the vortex core and forms a right-handed helix. **b**, Spatiotemporal power spectrum of the vortex-core radius S_a for $d = 7$ mm, a pump flow rate $U = 9$ V and no external forcing. Solid white lines correspond to the theoretical dispersion relation of equation (2) with $m = 2$, and parameters $a_0 = 2.2$ mm, $\Gamma = 0.011$ m^2 s^{-1} and $v_z = 0.85$ m s^{-1}, consistent with experimentally measured values. The solid red line corresponds to $\omega = kv_z$ and possibly indicates a soliton or another undetermined perturbation. To account for variations of the radius a with depth z, the white dashed lines correspond to equation (2) computed with $a_0 = \min[a(z)]$ (right) and $a_0 = \max[a(z)]$ (left).

We observe these $m = 2$ waves without forcing, as drain-hole flow temporal fluctuations suffice to perturb the core size. The vortex-core radius spectrum (Fig. 4b) reveals a clear dispersion relation crossing $f = 0$ near $|k|a_0 \approx 1$, consistent with a low phase velocity (Supplementary Video 2) and nearly stationary behaviour. Although theoretically challenging—fluted waves often involve instabilities and singular behaviour requiring intricate analytical approaches[29,30]—the experimental data

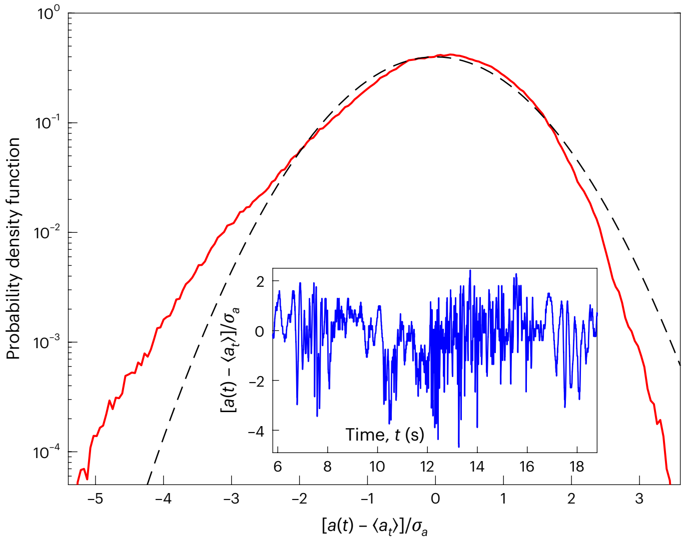

Fig. 5 | Probability distribution function of the temporal fluctuations of the normalized vortex-core radius, $[a(t) - \langle a \rangle_t]/\sigma_a$. $\sigma_a = \sqrt{\langle a^2 \rangle_t} = 0.1$ mm is the r.m.s. value, and $\langle a \rangle_t = 1.3$ mm, corresponding to $m = 2$ Kelvin waves. There is no external forcing. $d = 7$ mm, and $U = 6.8$ V. The dashed line is a normal distribution with zero mean and unit standard deviation. Inset: corresponding temporal fluctuations of the vortex-core radius, centred and reduced, $[a(t) - \langle a \rangle_t]/\sigma_a$. Measurement uncertainty on $a(t)$ is negligible.

matches equation (2) reasonably well (solid white lines in Fig. 4b) using $a_0 = 2.2$ mm, $\Gamma = 0.011$ m^2 s^{-1} and $v_z = 0.85$ m s^{-1}, consistent with experimental values (Methods). Again, the dashed white lines account for the variation of $a(z)$ within the measured range. The observed broadening of the branches could also be due to nonlinear wave interactions[34]. Note that these $m = 2$ waves are a priori absent in quantum turbulence, as they involve spatial scales comparable to the vortex core where hydrodynamics breaks down[35]. A weaker dispersion branch is also visible in Fig. 4b (solid red line), which is systematically consistent with $\omega = kV_z$ and possibly indicates a soliton or another undetermined perturbation.

Finally, although the hollow vortex in our set-up intrinsically includes a free surface that could, in principle, support capillary and centrifugal waves, our data show no evidence of these (Supplementary Information). At high k, surface tension is expected to modify Kelvin's dispersion[36,37]; however, as shown in Extended Data Fig. 5, our experimental parameter ranges render capillary effects negligible. At low k, the air–water interface can sustain centrifugal surface waves[38–40]. Distinct from Kelvin waves and driven by an effective gravity due to the centrifugal acceleration $g_{\mathrm{eff}} = \Omega_0^2 a_0$, these waves exist even without a vorticity filament and are systematically Doppler-shifted by the fluid rotation. However, these centrifugal waves do not match our measurements (Extended Data Fig. 6).

Discussion and conclusion

Our set-up enables a detailed characterization of Kelvin waves along a stable, rectilinear, free-surface vortex and closely reproduces a Rankine vortex. A key result is the striking agreement with the theory of equation (2) for helical ($m = 1$) and double-helix ($m = 2$) modes[1,28], but the scope of our findings goes well beyond the dispersion relation itself. We showed that a single macroscopic vortex supports several wave modes that propagate upstream and downstream. Notably, such spectral richness is made possible because our container is not rotating and thanks to our dedicated injection system; by contrast, earlier rotating set-ups attenuated the disturbances and prevented access to the Kelvin wave dispersion relation. The $m = 2$ waves show pronounced spectral broadening (Fig. 4b), indicating strong nonlinear interactions, unlike the more linear $m = 1$ bending waves (Fig. 3). This underlines the importance of $m = 2$ modes in small-scale dissipation and wave turbulence cascades theoretically predicted but never experimentally observed, and they could, thus, stimulate new developments. Similar structures have been predicted near $ka_0 \approx 1$ for $v_z = 0$ (ref. 29), indicating their relevance even when the vertical flow is weak.

The contrasting shape of the upstream and downstream $m = 1$ dispersion branches (Fig. 3c) highlights two key aspects: (1) the key role of vertical velocity near the vortex core, which controls the helicity of the flow[41], and (2) the influence of the source location on the shape of the dispersion relation, for either downstream or upstream waves, like gravity waves generated by obstacles in rivers[37]. Strong temporal fluctuations of the vortex radius ($m = 2$ mode) are observed (inset of Fig. 5). The centred, reduced probability distribution (Fig. 5) shows strong asymmetry (skewness $\langle a^3 \rangle / \langle a^2 \rangle^{3/2} = -0.45$), indicating that extreme radius reductions are more probable than enlargements because of the lower energy required to shrink the air core than to push into the liquid. By contrast, temporal fluctuations of the vortex displacement ($m = 1$ mode) are ten times slower and more intense and have a Gaussian distribution (Extended Data Fig. 7). These statistical features are not directly linked to the dispersion relation but reveal unexpected fluctuation dynamics and open promising avenues for the study of turbulence in vortical flows.

Our observations have broad implications for geophysical vortices, particularly for tornado dynamics during their final rope-like phase, as these closely resemble our set-up. Intense upward flows along tornado cores driven by convection or suction could generate two branches of the Kelvin wave dispersion relation. Depending on the disturbance origin (ground or aloft), waves may propagate up- or downstream, affecting the energy distribution, stability and trajectory. A key result reported here is the identification of an ascending $m = 1$ mode with vanishing group velocity near $|k|a_0 \approx 1$, which leads to localized energy trapping near the ground and triggers the 'skipping effect', namely intermittent vortex lifting or jumping. The strong fluctuations of the vortex position of such modes can also lead to abrupt lateral shifts in tornado trajectories. Moreover, skewed $m = 2$ double-helix fluctuations could drive sudden core airflow instabilities and contribute to the dynamics of suction vortices[8], which are small, disordered structures observed around tornado cores and are thought to play a large role in localized damage. These findings may have applications for the rope-like stage of tornadoes, with potential applications to forecasting models. In aircraft wake vortices, we predict that a strong axial flow could favour $m = 2$ modes near the core, thus influencing vortex stability and dissipation at subwingspan scales. This contrasts with the classic $m = 1$ Crow instability, which typically governs vortex evolution and breakdown[42].

Although our system is entirely classical, by offering a direct measurement still inaccessible in quantum systems, the universal nature of the Kelvin wave dispersion relation makes it relevant to superfluid contexts as well. The observed $m = 1$ mode is precisely that expected to dominate the turbulent cascade in quantum fluids, where Kelvin waves emerge from vortex reconnections[18]. Although this analogy must be drawn with care (as quantum vortices are topologically protected and involve core scales beyond hydrodynamic resolution), our results provide the first experimental validation of a key mechanism in quantum turbulence and shed light on energy transfer and dissipation.

Future work will explore weakly nonlinear interactions and the Kelvin wave turbulence regime predicted theoretically[19,20]. The coexistence of several dispersion branches may enable atypical nonlinear interactions[43]. Our system also offers a platform for investigating solitons on vortex filaments[44,45]. On the theoretical side, extending the local approach to account for the full axial evolution of the vortex structure, or even performing a direct numerical simulation or global linear stability analysis, would provide a more complete theoretical understanding of wave dynamics in confined vortices. This study also opens the way to observing interactions in a vortex array mediated by Tkachenko waves[46,47], which are collective modes of great relevance in various domains involving vortices.

Online content

Any methods, additional references, Nature Portfolio reporting summaries, source data, extended data, supplementary information, acknowledgements, peer review information; details of author contributions and competing interests; and statements of data and code availability are available at https://doi.org/10.1038/s41567-026-03175-w.

References

1. Thomson, W. Vibrations of a columnar vortex. *Philos. Mag.* **10**, 155–168 (1880).
2. Widnall, E. S. The structure and dynamics of vortex filaments. *Annu. Rev. Fluid Mech.* **7**, 141–165 (1975).
3. Pullin, D. I. & Saffman, P. G. Vortex dynamics in turbulence. *Annu. Rev. Fluid Mech.* **30**, 31–51 (1998).
4. Jiménez, J. & Wray, A. A. On the characteristics of vortex filaments in isotropic turbulence. *J. Fluid Mech.* **373**, 255–285 (1998).
5. Jacquin, L., Fabre, D., Sipp, D., Theofilis, V. & Vollmers, H. Instability and unsteadiness of aircraft wake vortices. *Aerosp. Sci. Technol.* **7**, 577–593 (2003).
6. Spalart, P. R. Airplane trailing vortices. *Annu. Rev. Fluid Mech.* **30**, 107–138 (1998).
7. Dahl, J. M. L. Centrifugal waves in tornado-like vortices: Kelvin's solutions and their applications to multiple-vortex development and vortex breakdown. *Mon. Weather Rev.* **149**, 3173–3216 (2021).
8. Davies-Jones, R., Trapp, R. J. & Bluestein, H. B. in *Severe Convective Storms* (ed. Doswell, C. A.) 167–221 (Springer Nature, 2001).
9. Maxworthy, T. A vorticity source for large-scale dust devils and other comments on naturally occurring columnar vortices. *J. Atmos. Sci.* **30**, 1717–1722 (1973).
10. Onsager, L. Statistical hydrodynamics. *Nuovo Cimento* **6**, 279–287 (1949).
11. Feynman, R. P. in *Progress in Low Temperature Physics* Vol. 1 (ed. Halperin, W. P.) Ch. 2 (Elsevier, 1955).
12. Salomaa, M. M. & Volovik, G. E. Quantized vortices in superfluid ^{3}He. *Rev. Mod. Phys.* **59**, 533 (1987).
13. Peretti, C., Cessaire, J., Ducrozoy, E. & Gibert, M. Direct visualization of the quantum vortex lattice structure, oscillations, and destabilization in rotating He-4. *Sci. Adv.* **9**, eadh2899 (2023).
14. Donnelly, R. J. *Quantized Vortices in Helium II* Vol. 2 (Cambridge Univ. Press, 1991).
15. Krstulovic, G. Kelvin-wave cascade and dissipation in low-temperature superfluid vortices. *Phys. Rev. E* **86**, 055301 (2012).
16. Vinen, W. F. & Niemela, J. J. Quantum turbulence. *J. Low Temp. Phys.* **128**, 167–231 (2002).
17. Glaberson, W. I., Johnson, W. W. & Ostermeier, R. M. Instability of a vortex array in He II. *Phys. Rev. Lett.* **33**, 1197 (1974).
18. Kivotides, D., Vassilicos, J. C., Samuels, D. C. & Barenghi, C. F. Kelvin waves cascade in superfluid turbulence. *Phys. Rev. Lett.* **86**, 3080–3083 (2001).
19. L'vov, V. S. & Nazarenko, S. Weak turbulence of Kelvin waves in superfluid He. *Low Temp. Phys.* **36**, 785 (2010).
20. Kozik, E. & Svistunov, B. Kelvin-wave cascade and decay of superfluid turbulence. *Phys. Rev. Lett.* **92**, 035301 (2004).
21. Clark di Leoni, P., Mininni, P. D. & Brachet, M. E. Spatiotemporal detection of Kelvin waves in quantum turbulence simulations. *Phys. Rev. A* **92**, 063632 (2015).
22. Mäkinen, J. T. et al. Rotating quantum wave turbulence. *Nat. Phys.* **19**, 898–903 (2023).
23. Fonda, E., Meichle, D. P., Ouellette, N. T., Hormoz, S. & Lathrop, D. P. Direct observation of Kelvin waves excited by quantized vortex reconnection. *Proc. Natl Acad. Sci. USA* **111**, 4707 (2014).
24. Minowa, Y. et al. Direct excitation of Kelvin waves on quantized vortices. *Nat. Phys.* **21**, 233–238 (2025).
25. Maxworthy, T., Hopfinger, E. J. & Redekopp, L. G. Wave motions on vortex cores. *J. Fluid Mech.* **151**, 141–165 (1985).
26. Hopfinger, E. J. & Browand, F. K. Vortex solitary waves in a rotating, turbulent flow. *Nature* **295**, 393–395 (1982).
27. Kleckner, D. & Irvine, W. T. M. Creation and dynamics of knotted vortices. *Nat. Phys.* **9**, 253–258 (2013).
28. Saffman, P. G. *Vortex Dynamics* (Cambridge Univ. Press, 1992).
29. Fabre, D., Sipp, D. & Jacquin, L. Kelvin waves and the singular modes of the Lamb-Oseen vortex. *J. Fluid Mech.* **551**, 235–274 (2006).
30. Le Dizès, S. & Lacaze, L. An asymptotic description of vortex Kelvin modes. *J. Fluid Mech.* **542**, 69–96 (2005).
31. Andersen, A., Bohr, T., Stenum, B., Rasmussen, J. J. & Lautrup, B. Anatomy of a bathtub vortex. *Phys. Rev. Lett.* **91**, 104502 (2003).
32. Andersen, A., Bohr, T., Stenum, B., Rasmussen, J. J. & Lautrup, B. The bathtub vortex in a rotating container. *J. Fluid Mech.* **556**, 121–146 (2006).
33. Inui, S., Nakagawa, T. & Tsubota, M. Bathtub vortex in superfluid ^{4}He. *Phys. Rev. B* **102**, 224511 (2020).
34. Krstulovic, G. *A Theoretical Description of Vortex Dynamics in Superfluids. Kelvin Waves, Reconnections and Particle Vortex Interaction*. HDR thesis, Univ. Côte d'Azur (2020).
35. Roberts, P. H. On vortex waves in compressible fluids. I. The hollow-core vortex. *Proc. R. Soc. Lond. Ser. A* **459**, 331–352 (2003).
36. Binnie, A. M. The theory of waves travelling on the core in a swirling liquid. *Proc. R. Soc. Lond. Ser. A* **205**, 530–540 (1951).
37. Keller, J. J. & Escudier, M. P. Theory and observations of waves on hollow-core vortices. *J. Fluid Mech.* **99**, 495–511 (1980).
38. Phillips, O. M. Centrifugal waves. *J. Fluid Mech.* **7**, 340–352 (1960).
39. Miles, J. W. & Troesch, B. A. Surface oscillations of a rotating liquid. *J. Appl. Mech.* **28**, 491–496 (1961).
40. Batchelor, G. K. *An Introduction to Fluid Dynamics* (Cambridge Univ. Press, 1967).
41. Moffatt, H. K. The degree of knottedness of tangled vortex lines. *J. Fluid Mech.* **35**, 117–129 (1969).
42. Crow, S. C. Stability theory for a pair of trailing vortices. *AIAA J.* **8**, 2172–2179 (1970).
43. Novkoski, F., Pham, C.-T. & Falcon, E. Evidence of experimental three-wave resonant interactions between two dispersion branches. *Phys. Rev. E* **107**, 045101 (2023).
44. Hasimoto, H. A soliton on a vortex filament. *J. Fluid Mech.* **51**, 477–485 (1972).
45. Hopfinger, E. J., Browand, F. K. & Gagne, Y. Turbulence and waves in a rotating tank. *J. Fluid Mech.* **125**, 505–534 (1982).
46. Sonin, E. B. Tkachenko waves. *JETP Lett.* **98**, 758–768 (2014).
47. Coddington, I., Engels, P., Schweikhard, V. & Cornell, E. A. Observation of Tkachenko oscillations in rapidly rotating Bose–Einstein condensates. *Phys. Rev. Lett.* **91**, 100402 (2003).

Methods

This section is divided into three parts. The first part describes the experimental set-up, the second part details the measurement techniques and the third one the data analysis.

Experimental set-up

The experiment was specifically designed to enable the direct measurement of the Kelvin wave dispersion relation over two decades in frequency and wavenumber. The experiment consists of a rectangular tank with dimensions 50 cm × 50 cm × 50 cm in which a stationary bathtub vortex is generated and drains out through a circular hole at the bottom (Fig. 1). The use of a bathtub-type vortex with a central air core provides a sharp optical interface, enabling precise, time-resolved tracking of the shape and position of the vortex filament. Water is injected at four symmetrically positioned inlets around the hole using two LVM117 pumps (24 V and 2.5 A) operating at a controlled rate. The drained water is collected in an external basin and recirculated by the pumps. This injection mechanism promotes the generation of Kelvin waves, which are typically suppressed in conventional bathtub vortex set-ups in which the whole tank is rotated. To enhance vortex formation and stability, a Plexiglas cylinder with a height of 45 cm and a diameter of 21 cm is positioned around the vortex. Near the top region, where the vortex expands to meet the horizontal free surface at the top of the tank, an annulus with a diameter of 14 cm is immersed at a depth $z = 3$ cm around the vortex. This annulus is connected to a shaker that generates low-frequency horizontal oscillations (sweeping between 1 Hz and 6 Hz for the data reported here) to force downward waves along the vortex line without causing the filament to break up or a loss of coherence.

Measurement techniques

The air–water interface of the vortex was imaged using an optical camera (Basler acA2040-120um, 2,064 × 1,564 px^2) positioned normal to the vortex axis and two light panels. Reflected light at the interface created a sharp white contour, which enabled accurate spatiotemporal measurements of the vertical profile of the vortex. Videos were captured with two camera lenses (8 mm wide-angle and 12 mm small-angle) to provide complementary views of the vortex. To compute the spatiotemporal spectra, the vortex profile was measured over $L = 12.5$ cm in z centred around a depth $z = 22$ cm, leading to a wavenumber resolution of $8 \times 2\pi$ m^{-1}. The horizontal and vertical resolutions were 60 µm px^{-1}, whereas the contour width was 0.5 mm, which resulted in a typical measurement uncertainty on the core radius and position of about 0.1 mm.

The typical acquisition frequency was 300 fps, with recordings lasting $T = 30$ s. Image postprocessing (contour detection) extracted the left-hand and right-hand vortex profiles used to compute the vortex-core position $\eta(z,t) = [r(z,t,\theta=0) - r(z,t,\theta=\pi)]/2$ and vortex-core radius $a(z,t) = [r(z,t,\theta=0) + r(z,t,\theta=\pi)]/2$. These signals were analysed in Fourier space to study the dispersion relation of Kelvin waves. The spatiotemporal spectra $S_X(\omega,k) = |\widetilde{X}(\omega,k)|^2/LT$ in m^3 s^{-1} (where $\widetilde{X}$ is the two-dimensional Fourier transform of $X(z,t)$, X being either η or a) of the left-hand and right-hand profiles both feature every mode m. By computing the vortex-core position and radius from these profiles, we selected, respectively, either the $m = 1$ mode or all the other modes ($m = 0, 2, 3, \ldots$).

We used PIV for the fluid velocity measurements[48]. A laser beam, shaped into a planar sheet using a Powell lens, illuminated 10-µm-diameter hollow glass particles suspended in the fluid. The particles scattered the laser light, which enabled the visualization of their motion from above within a selected horizontal plane using a high-speed camera (Phantom V1840) operating at 6,000 fps. The seeding particles have Stokes number St ≈ 0.1, which ensured their tracer-like behaviour[48] and negligible influence on the vortex dynamics, including near the small drain hole. This approach allowed us to capture detailed velocity fields with minimal averaging effects, as the acquisition time (0.1 s) was much shorter than the typical vortex wandering time. Images were processed in MATLAB using the PIVlab software, which produced velocity data on a 37 × 23 grid with a 2.7-mm spatial resolution. The resulting fluid velocity fields were used to compute (after averaging over θ) the azimuthal velocity profile $v_\theta(r)$, which is essential for characterizing the vortex dynamics, and to access key experimental parameters such as the circulation $\Gamma = 2\pi r v_\theta(r)$. Flow fluctuations and resolution limits near the axis led to typical measurement uncertainties on the circulation of approximately 0.005 m^2 s^{-1}.

The vertical fluid velocity profile $v_z(z)$ was measured by particle-tracking velocimetry at $r = a(z)$. We tracked the motion of 1.5-mm-diameter expanded-polystyrene particles (which have a density close to that of water) seeded near the top core of the vortex. We then used the same imaging technique used for the above contour detection measurements to track their advection along the vortex core, with typical measurement uncertainties of $\delta v_z \approx 0.05$ m s^{-1}.

Fitting technique and analysis

The fitting technique was the same for Figs. 3b,c, and 4b. We used the measured value of $a_0 = \langle a(z) \rangle_z$ from Extended Data Fig. 4, then we fitted the data with equation (2) using the best couple of parameters (Γ, v_z). We checked a posteriori that this couple of parameters was consistent with the measured values from Extended Data Figs. 2 and 3. Although the vortex-core radius $a(z)$ varied substantially along the z axis, the measured dispersion relation remained in strong agreement with the uniform-core theoretical prediction of equation (2). This robustness can be attributed to a WKBJ-type local approximation, in which the wavenumber adapts continuously to the slowly varying structure of the vortex. Such an approach, widely used for slowly varying media[49], justifies the use of local dispersion relations despite axial variations of the vortex core and explains some of the broadening observed in our experimental data. This spectral broadening induced by axial variations of the vortex radius was roughly estimated. Assuming $ka_0 \ll 1$ and constant ω along the propagation, differentiating the classical Kelvin dispersion relation (equation (1)) yields a relation between the typical variations of $k(z)$ and $a(z)$:

$$\frac{\delta k}{k_0}\left[2\log\left(\frac{2}{k_0 a_0}\right) - 1 - 2\gamma\right] = \frac{\delta a}{a_0}.$$

This expression provides a first-order estimate of the wavenumber broadening Δk due to axial inhomogeneity of the vortex core. For typical values $k_0/2\pi = 25$, $\delta a = 1$ mm and $a_0 = 1.9$ mm, it yields $\Delta k/(2\pi) \approx 8$ m^{-1}, consistent with our observations in Fig. 3b,c at small k, where the dashed curves were obtained from the full dispersion relation (equation (2)) that is valid for all k. Naturally, a more advanced theoretical framework would be required to fully capture this effect. Future work will involve global stability analyses or even direct numerical simulations of the full set-up and explicitly account for the axial variability of the base flow and use realistic boundary conditions. In particular, because the axial profile of $a(z)$ reflects the structure of the pressure field, which is itself influenced by the propagating waves, the problem becomes intrinsically nonlinear and complex. Although such developments lie beyond the scope of the present study, they will be the subject of future investigations.

To compute the probability density functions, the signal $a(z,t)$ or $\eta(z,t)$ was recorded over 10 min at 100 fps or 3 min at 360 fps, respectively, then sliced into 1,000 discrete values of z over 2.5 cm in height (centred around $z = 18$ cm) and concatenated in a single temporal file for $a(t)$ or $\eta(t)$.

Data availability

The data that support the findings of this study, including the data used to compute the spatiotemporal power spectra, are available via figshare at https://doi.org/10.6084/m9.figshare.30903347 (ref. 50).

References

48. Raffel, M., Willert, C. E., Wereley, S. T. & Kompenhans, J. *Particle Image Velocimetry: A Practical Guide* 3rd edn (Springer, 2018).
49. Whitham, G. B. *Linear and Nonlinear Waves* (Wiley-Interscience, 1974).
50. Barckicke, J., Falcon, E. & Gissinger, C. Data for: Kelvin wave propagation along vortex core. *figshare* https://doi.org/10.6084/m9.figshare.30903347 (2025).

Acknowledgements

We thank A. Di Palma and Y. Le Goas for technical support. We thank B. Semin for providing polystyrene particles and J.-B. Gorce for discussions on PIV. E.F. acknowledges support from the Simons Foundation MPS (Grant No. 651463, Wave Turbulence, USA) and the French National Research Agency (Sogood Project No. ANR-21-CE30-0061-04, Lascaturb Project No. ANR-23-CE30-0043-02 and Provebact Project No. ANR-24-CE09-1394-02). C.G. acknowledges financial support from the French programme 'JCJC' managed by the French National Research Agency (MagnetDrive Project No. ANR-19-CE30-0025-01) and the Institut Universitaire de France.

Author contributions

C.G. conceived of the experiment and designed the set-up with feedback from E.F. and J.B. E.F. led the implementation of the experimental measurements. J.B. and E.F. built the apparatus. J.B. conducted the experiments and performed the data analysis. E.F. received the funding. All authors contributed to the theoretical framework and interpretation of the experimental results. C.G. wrote the first draft of the paper, with substantial input, figures and revisions from J.B. and E.F. All authors outlined the content of the paper and reviewed and edited the paper.

Competing interests

The authors declare no competing interests.

Additional information

Extended data is available for this paper at https://doi.org/10.1038/s41567-026-03175-w.

Supplementary information The online version contains supplementary material available at https://doi.org/10.1038/s41567-026-03175-w.

Correspondence and requests for materials should be addressed to Eric Falcon or Christophe Gissinger.

Peer review information *Nature Physics* thanks Daniel Lathrop and the other, anonymous, reviewer(s) for their contribution to the peer review of this work.

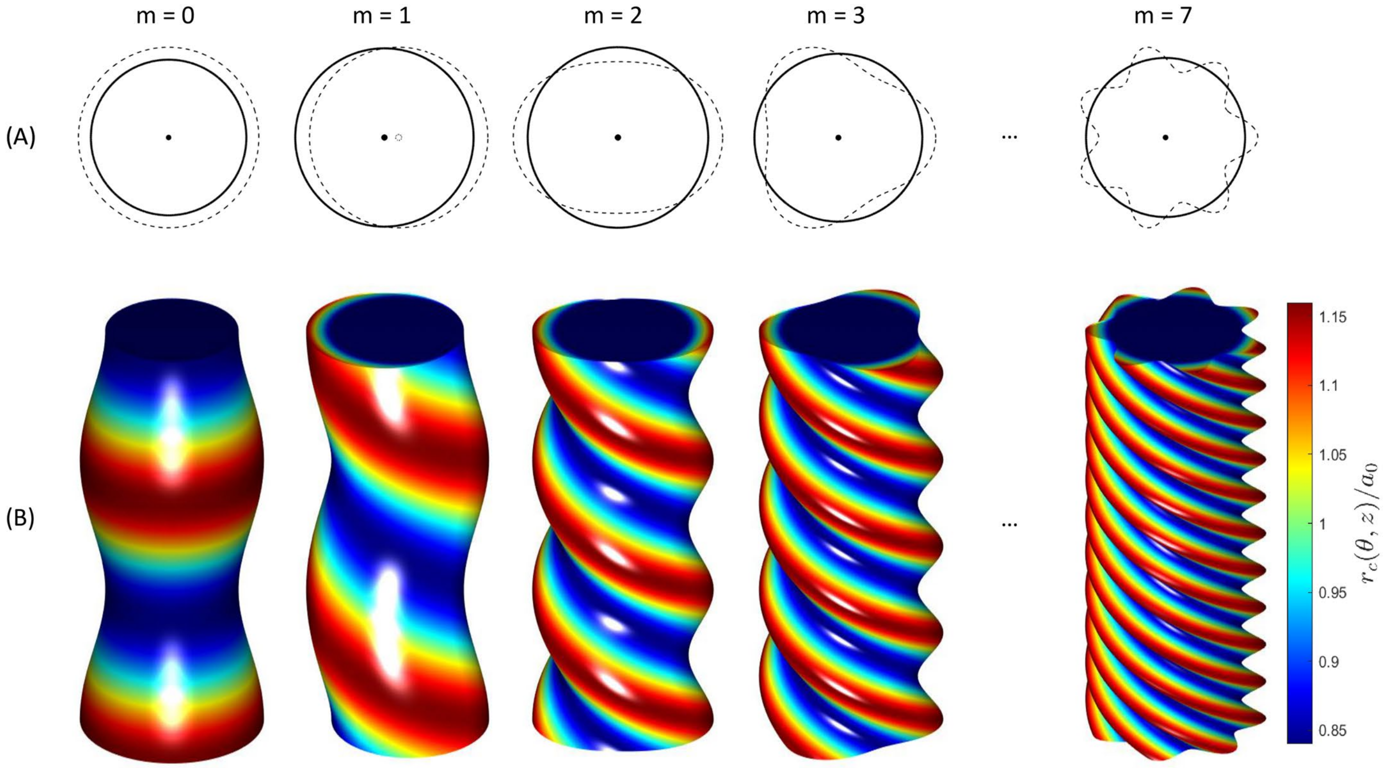

Extended Data Fig. 1 | Theoretical azimuthal deformations of a vortex line for different Kelvin wave modes. For azimuthal wavenumbers $m = 0, 1, 2, 3$, and 7: (**A**) Top view, (**B**) Lateral view. Only the $m = 1$ mode displaces the vortex axis and has no radius variation.

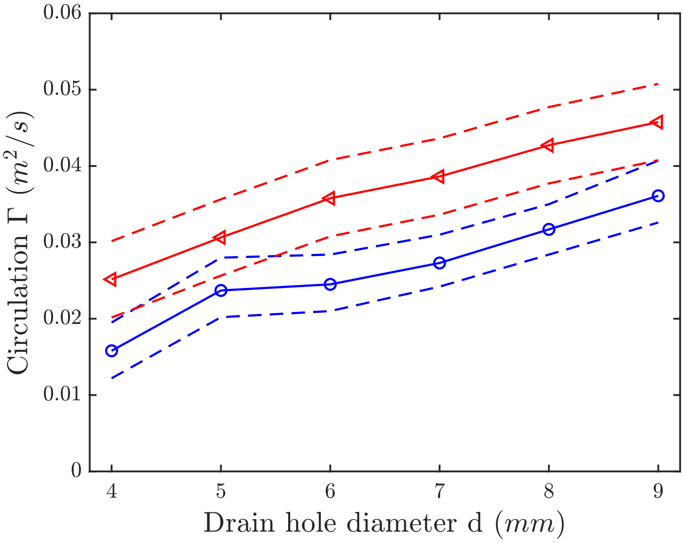

Extended Data Fig. 2 | Experimental circulation $\Gamma = 2\pi r v_\theta(r)$ as a function of the drain hole diameter *d*. (red curve, triangles): Γ measured by PIV in a horizontal plane located at a depth of $z = 25$ cm and near $r \sim 1$ cm. Dotted lines show uncertainty of measurements and variability in z: $\delta\Gamma \simeq 5.10^{-3} m^2/s$. (blue curve, circles): Γ inferred by fitting data with the solid rotation Rankine model with a_0 and v_z measured as in Fig. 2b and Extended Data Fig. VerticalVelocity, respectively. Dotted lines correspond to the same fit, but with a_0 taking the values of $a(z)$ at the bottom and at the top of the measured range (below and above, respectively). $U = 11$ V.

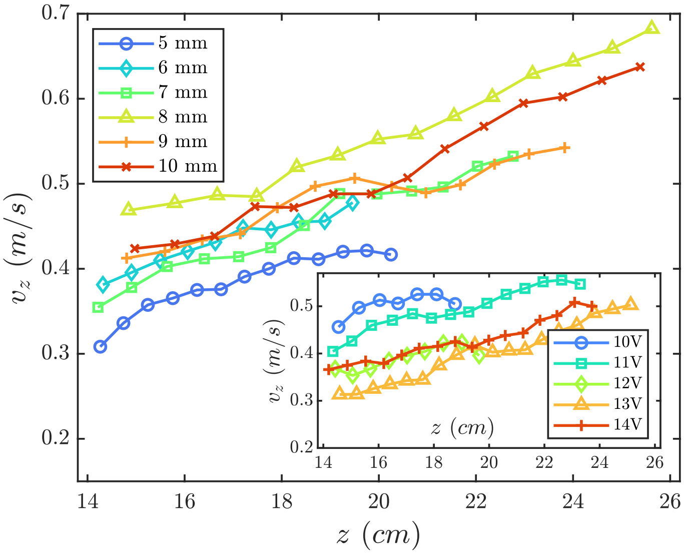

Extended Data Fig. 3 | Experimental downward vertical velocity v_z as a function of the depth *z*. Measured from the flat free surface ($z = 0$) for different drain hole diameters *d*. v_z is measured by PTV at $r = a(z)$. $U = 11$ V. Inset: Same for different pump flow rates *U* for $d = 7$ mm. Measurement uncertainty is $\delta v_z \simeq 0.05 m/s$. It is not shown on the graph for the sake of clarity - note that it is smaller than the variations in *z*.

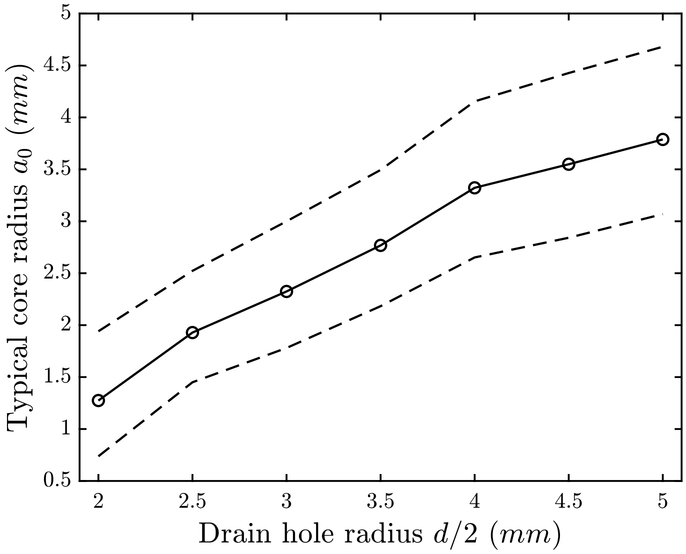

Extended Data Fig. 4 | Experimental vortex-core radius a_0 as a function of the drain hole radius $d/2$. Dotted lines indicate the values of $a(z)$ at the bottom and top of the measured range. The mean radius $a_0 = \langle a \rangle_z$ is obtained by contour detection and averaged over the vertical camera field $z \in [15.5, 28]$ cm. $U = 11$ V. Measurement uncertainty is negligible.

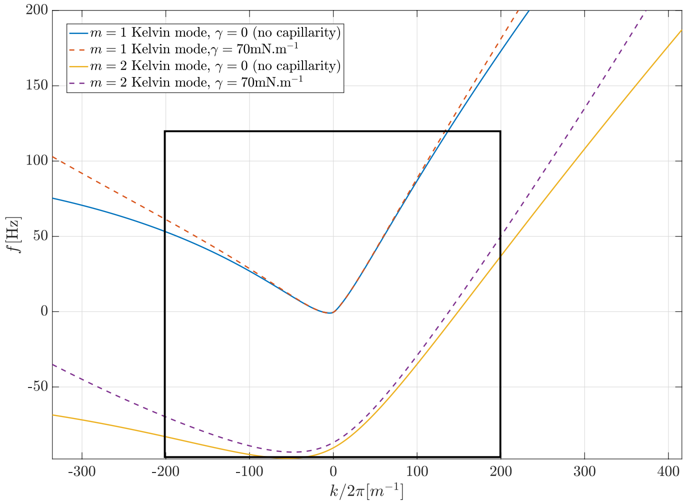

Extended Data Fig. 5 | Hollow–core model with and without surface tension. for $m = 1$ and $m = 2$ Kelvin modes, with parameters $V_z = 0.3$m/s, $\gamma = 70$mN/m, $a_0 = 1.9$ mm, and $\Gamma = 0.022$. In our range, capillary corrections remain negligible compared to our experimental uncertainties. The black square marks the typical range of our experimental measurements.

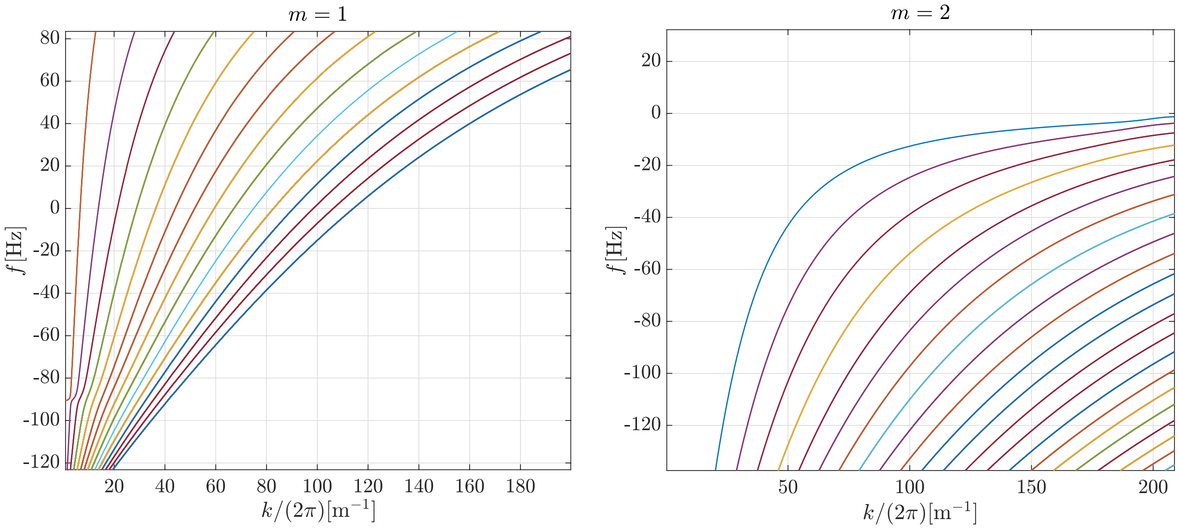

(a) (b)

Extended Data Fig. 6 | Theoretical $m = 1$ (a) and $m = 2$ (b) centrifugal waves from Phillips' dispersion relation. with experimental parameters $a_0 = 1.9$ mm, $\Gamma = 0.022$ and $c = 0.05$. Different curves correspond to different zeros of the Bessel functions. No agreement is found with the experimental dispersion relations reported here, as $m = 1$ solutions are always far from $(\omega, k) \approx (0, 0)$ and $m = 2$ modes never cross $f = 0$ in the experimental range.

https://doi.org/10.1038/s41567-026-03175-w

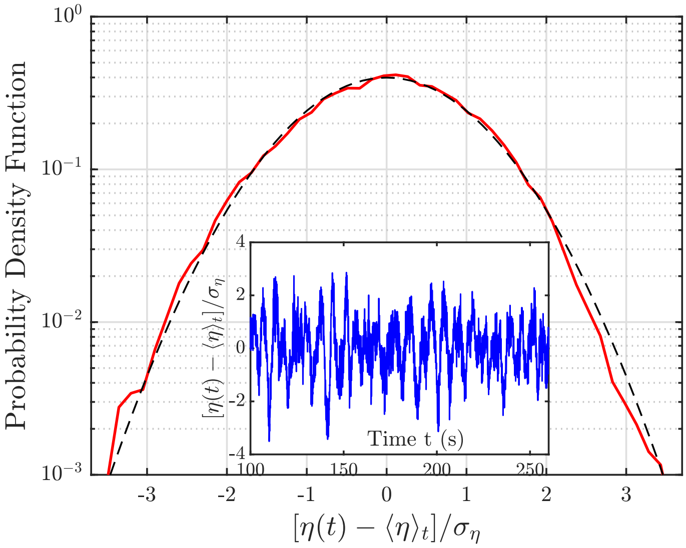

Extended Data Fig. 7 | Probability distribution function (PDF) of the temporal fluctuations of the normalized vortex-core position, $[\eta(t) - \langle\eta\rangle_t]/\sigma_\eta$. $\sigma_\eta = \sqrt{\langle\eta^2\rangle_t} = 1.2$ mm is the rms value, corresponding to $m = 1$ bending Kelvin waves. $\sigma_\eta = \sqrt{\langle\eta^2\rangle_t} = 1.2$ mm is the rms value. Sweep-sine forcing. $d = 7$ mm, $U = 6.8$ V. Dashed line: Normal distribution of zero mean and unit standard deviation. Inset: corresponding temporal fluctuations of the vortex-core. Measurement uncertainty on η is negligible.